
Article:
Vincent, J.D.S., Leong, Z. and Morley, N.A. orcid.org/0000-0002-7284-7978 (2024) Interpretation of magnetostrictive sensor data in Mode 1 and Mode 2 of carbon fibre reinforced polymers. Sensors and Actuators A: Physical, 365. 114888. ISSN 0924-4247

https://doi.org/10.1016/j.sna.2023.114888

Sensors & Actuators: A. Physical 365 (2024) 114888

Contents lists available at ScienceDirect

Sensors and Actuators: A. Physical

journal homepage: www.journals.elsevier.com/sensors-and-actuators-a-physical

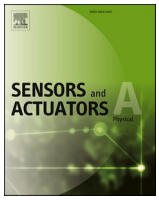

Interpretation of magnetostrictive sensor data in Mode 1 and Mode 2 of carbon fibre reinforced polymers

Jamin Daniel Selvakumar Vincent [a,b], Zhaoyuan Leong [a], Nicola A. Morley [a,*]

[a] Department of Materials Science and Engineering, University of Sheffield, Sheffield, United Kingdom
[b] National Physical Laboratory, Hampton Road, Teddington, Middlesex, TW11 0LW, United Kingdom

ARTICLE INFO

Keywords:
Structural health monitoring
Carbon-fibre reinforced polymers
End-notch failure
Double Cantilever Beam

ABSTRACT

Structural health monitoring (SHM) of carbon fibre reinforced polymers (CFRP) provides a valuable way to assess the condition of these materials, which possess desirable traits, but exhibit little elastic failure. Further complications arise due to their multi component nature, which means they can fail in a variety of ways. High-fidelity magnetostrictive SHM technology exhibits higher cost when utilising top-end materials that contain rare-earth elements. At the expense of fidelity, cost can be reduced by using Fe-based ribbons and cheap transducers. This reduction in accuracy can be overcome by coupling a detection array with the development of specific detection schemes for each failure type to reduce signal complexity. In this work, we investigate the failure of CFRP coupons in Mode 1 and 2 failure, using FeSiB ribbons as the actuator either bonded between the CFRP ply or co-cured on the surface. During the measurement, a set of 4 pancake coils are used to measure the change in inductance, as the CFRP fails, thus demonstrating that this magnetostrictive-coil set-up can be used to measure cracks forming and propagating within the CFRP, hence it is a promising SHM system. For the first time, it is demonstrated that there is a correlation between the induction signal and the elastic energy stored within the CFRP coupon.

1. Introduction

Due to increasing demand in the aviation industry worldwide coupled with the decreasing marginal fuel efficiency improvements means that the relative carbon footprint of this industry is expected to increase in the future [1]. Composite materials such as carbon fibre reinforced polymers (CFRP) are an obvious route for light weighting aerospace components. The Airbus A380 and Boeing 777 introduced in 1995/2005 have a structural mass of 20 % CFRP composites. Recent models such as the Boeing 787 and Airbus A350 introduced in 2011/2015 have structural mass 50 % CFRP composite. Although aerospace composites are now widely used commercially, it is not normal for an entire airframe to be built from these materials [2].

Metallic materials being homogenous have high ductility and clear fatigue characteristics. As a result, their crack propagation can be predicted reliably; CFRP materials are brittle because of their anisotropy and large scattered properties [3]. Although CFRP materials have been found to be more sensitive to impact damage, there is no clear understanding of the damage propagation mechanism. Due to this, parts design follow a “no-growth” approach where structures are designed to avoid damage during normal operation [4]. Therefore, for primary structures in FAR-25 and JAR-25 compliant aircraft, accidental damage becomes the primary concern in damage tolerance design and maintenance planning.

From the FAA Advisory on Composite Aircraft Structure [5], for any joint, the failure at which would result in catastrophic loss of the aeroplane, the limit load capacity must be addressed by one of the following ways: 1) Disbonds greater than the maximum load must be prevented by design features, 2) Testing of each individual production piece to determine its critical limits, 3) Repeatable and reliable non-destructive testing to ensure continued strength of the joint. It may be expected that although current non-destructive testing cannot meet criteria (3), the development of smart CFRP materials that enable structural health monitoring (SHM) could be met [6–8].

Magnetostrictive sensors were previously investigated as a potential SHM technology [9–13]. Recently, a damage detection system utilising a sparse array of magnetostrictive actuators was developed in order to use cost-efficient Fe-based materials in comparison to the higher sensitive, more expensive rare-earth magnetostrictive materials [9]. Although initial results were promising, the strain sensitivity resolution of the

* Corresponding author.
E-mail address: n.a.morley@sheffield.ac.uk (N.A. Morley).

https://doi.org/10.1016/j.sna.2023.114888
Received 12 May 2023; Received in revised form 8 November 2023; Accepted 28 November 2023
Available online 30 November 2023

Fe-based system was an order of magnitude less sensitive than piezoelectric sensors [14] and two orders less sensitive than Bragg gratings [15,16], but were still a promising option, due to other advantages including cost and easier attachment to the CFRP. Further other research has used magnetostrictive patches as transducers to produce Lamb waves within the CFRP composite to detect damage analogues to the piezoelectric sensors [17,18]. Thus these magnetostrictive sensors have to be further tested to understand their response to different failure modes, before a final decision on whether they are suitable for SHM of CFRP components can be made.

The other major difficulty faced by the aerospace industry to achieve SHM is the location and placement of these sensors on the CFRP component. Several placement methods have been investigated in the past such as placing the sensors between plies during layup [19–25], ply cut-out embedding [26,27] and interlacing sensors with reinforcement [23]. Embedding sensors between plies is considered as a flaw, since it creates discontinuities within the CFRP coupon, but there is no evidence that the initial damage was caused by the sensor embedding procedure under static and fatigue loading [19,27,28]. In this work two types of magnetostrictive actuator embedding have been investigated, including on the surface and between the 8th and 9th ply, as previous work [11] has found no visible voids around embedded magnetostrictive ribbons.

Interlaminar fracture is one of the major failures observed in CFRP materials. This failure occurs as a result of debonding/delamination between the plies. These damages can lead to catastrophic failure since the damage is not visible to visual inspection unlike impact damage. Interlaminar delamination leads to loss of strength of the material and stiffness [29,30]. There are three interlaminar fracture types that may occur in CFRP that correspond to the three principal axes: here termed Mode 1 (Opening), Mode 2 (In-plane shear), and Mode 3 (Out-of-plane shear) fracture [31,32]. Crack initiation occurs when critical stresses are reached within the component, followed by crack propagation along the crack path. The transient strain evolution at any particular point in a CFRP panel is a function of both the force experienced as well as the physical characteristics of the sample under load (*e.g.* elastic tensors). SHM uses actuators and sensors to measure this strain field within the CFRP, thus the strain field experienced at each sensor can be expressed as a function of time, $f(t)$, where t is time.

The material's stress response before and leading up to crack initiation and growth can be treated as a single event; as the effective range of each sensor is finite and the crack grows as a function of t, each sensor experiences the onset of this event at different periods *e.g.* $f(t), f(t+n_1), f(t+n_2)$ and so on. For the magnetostrictive SHM, this is measured as a change in the inductance response from the magnetostrictive actuator. Understanding and interpreting magnetostrictive sensor data responses with respect to different applied stresses will provide context for the development of damage detection schemas, whether through machine learning algorithms or as rules of thumb and is therefore the objective of this work.

2. Design of experiment

In order to investigate the effect of different CFRP failure mechanisms on the response of the magnetostrictive sensors, a design of experiment was carried out (Table 1). For each failure mode (Mode 1 and Mode 2), 12 samples were fabricated, this included two control samples, which contained no magnetostrictive ribbons, five samples with the magnetostrictive ribbons bonded between two of the ply and five samples with the magnetostrictive ribbons co-cured on the surface. This allowed for any statistical variation to be observed, and the main trends within the measurement to be identified. This allows us to be confident in the reliability of our measurements, even though the sensitivity of the magnetostrictive actuator-sensor is lower than other SHM systems.

Table 1
Experimental design of the actuator/sensor study performed.

Type of failure	Actuator placement	Number of samples
Mode 1 (Inter laminar fracture due to matrix failure under tensile loading)	No actuator/ribbons	2
	$Fe_{78}Si_7B_{15}$ ribbons between 8th and 9th ply	5
	$Fe_{78}Si_7B_{15}$ ribbons over the top surface of CFRP	5
Mode 2 (Inter laminar fracture due to matrix failure under shear loading)	No actuator/ribbons	2
	$Fe_{78}Si_7B_{15}$ ribbons between 8th and 9th ply	5
	$Fe_{78}Si_7B_{15}$ ribbons over the top surface of CFRP	5

3. Methodology

3.1. Synthesis

For the experiment, twill weave carbon fibre prepreg VTC 401 supplied by SHD Composites Ltd [33] with a ply thickness of 0.28 mm was used. The CFRP laminates were made up of 16 plies to achieve the required thickness for fracture testing. Using a release film, an initial delamination of 50 mm was initiated between 8th and the 9th ply. The laminates were fabricated on a flat plate mould of 400 mm × 450 mm. The laminates dimensions were 330 mm × 330 mm. FeSiB ribbons were co-cured along with the laminates either on their top or between 8th and 9th ply. The laminates were maintained in a vacuum of –29 mm/Hg. After vacuum bagging the laminate was placed inside an autoclave. The curing cycle was initiated with an initial ramp till 60 °C was reached with a ramp rate of 3 °C/min. Then the temperature was held at 60 °C for 60 min, before being ramped up till 120 °C with a rate of 3 °C/min. It was then allowed to dwell at 120 °C for 60 min. After which the laminate was allowed to cool down to room temperature.

3.2. Sample preparation

The samples were cut into 150 × 25 mm as per ASTM D5528 [34] and ASTM D 7909 [35] for Mode 1 and 2 tests using a tile cutter. Hasp and staples were adhesively bonded to the pre-cracked edge of the sample for Mode 1 test samples. The lateral sides of the laminates were painted to get a clear view of the crack propagation during testing. The sample was marked with 1 mm scale to keep a track of the crack growth. Schematics for the sample preparation are shown in Fig. 1(a) and (b).

3.3. Sensors and data acquisition system

An air cored pancake copper coil was used as a sensor to detect the change in inductance. A set of copper coils of diameter 0.224 mm were wound with 70 turns around a M3 washer in a clockwise direction. Similar pancake coils have been used for measuring inductance (L) of magnetostrictive actuators previously [36,37]. From [9], it was determined that these sensors had a sensitivity limit of 0.01 μStrain. A data acquisition system was developed based on a resistance-inductance-capacitance (RLC) circuit, which was used to measure the change in inductance of the magnetostrictive actuator. The RLC circuit can be described by the following equation:

$$q = Q_m e^{\frac{-t}{\tau}} \cos(\omega_D t + \phi) \quad (1)$$

Where q is the charge on the capacitor plates, is the exponential decrease of the oscillations amplitude, $\omega_D = \frac{1}{2L}\sqrt{\left[\frac{4L}{C} - (R)^2\right]}$ is the damped frequency, where L is the inductance, C is the capacitance and R is the resistance. For these measurements, the capacitor is chosen so that the system stays in an underdamped state, *i.e.* $R < \sqrt{\frac{4L}{C}}$. Thus with the

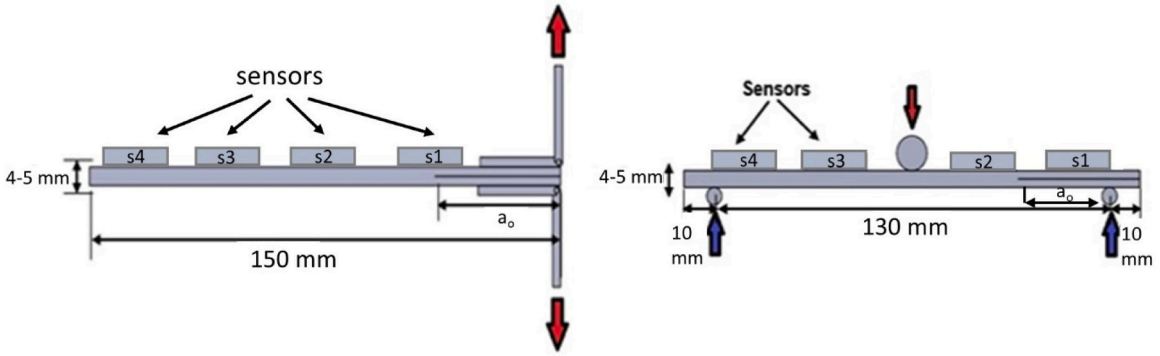

Fig. 1. **(a)** Schematic representation Mode 1 sample with dimensions **(b)** Schematic representation Mode 2 sample with dimensions.

resistance and the capacitance known for the circuit, any difference in the measured output will be due to a change in inductance in the coil. The design and development of the sensors and data acquisition system have been discussed extensively in the previous publication [9]. This includes how the capacitor in the RLC circuit was chosen, along with reducing the noise on the data compared to the inductance signal measured, this maximising the signal to noise (SNR) ratio.

3.4. Sensor position

To get more meaningful data for analysis the sensors were maintained in the same position for Mode 1 and Mode 2 testing exactly on top of the actuator. The first sensor (S1) was placed at 30 mm from the sample with the initial crack (right edge in Fig. 1). The second sensor (S2) was placed at 60 mm, the third sensor (S3) was placed at 90 mm and the fourth sensor (S4) was placed at 120 mm from the sample end with the initial crack.

4. Mechanical testing

The Mode 1 and Mode 2 fracture tests were carried out in a Hounsfield universal testing machine (UTM). The test coupons along with the attached inductive sensors were connected to the data acquisition system. To find the crack position at any instantaneous moment of time a Canon 80D camera was used to record the crack propagation during testing. Fig. 2 shows the schematic representation of the test along with the data acquisition process. The testing methodologies for Mode 1 and Mode 2 fracture tests were as follows:

1) For Mode 1 fracture tests as per ASTM D 5528 the Double Cantilever Beam (DCB) test method was used. A load cell of 100 kN was used to apply a tensile load on the CFRP coupon at the rate of 2 mm/min. The data from the sensors were recorded using the Arduino based data acquisition system. The data from the video camera was used to record the crack propagation and to correlate the sensor data with the crack length and the load data from the UTM.
2) For Mode 2 Fracture testing (End Notch Flexure) test method has been used as per ASTM D 7909. The sample was fixed to a three-point bending fixture in the UTM. A load cell of 10 kN was used to apply a bending load to the laminate at a loading rate of 2 mm/min. The data from the sensors was recorded using the Arduino based data acquisition system. Similar to Mode 1 tests, a camera was used to record the crack propagation data.

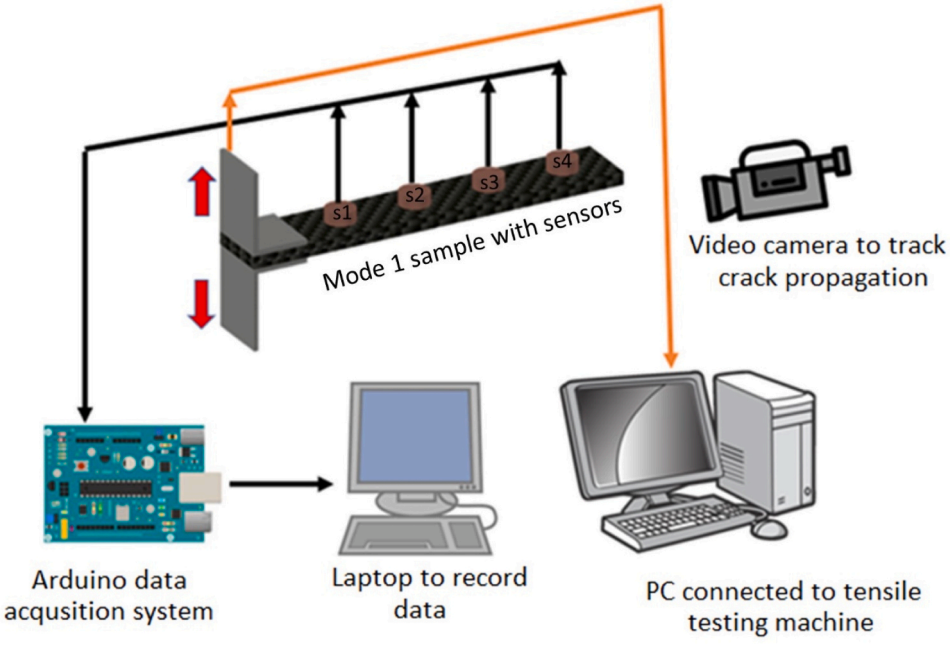

Fig. 2. Schematic representation of the experimental setup.

5. Results

For each measurement, there are three data sets, all measured as a function of time. These are the sensor measurement of the change in inductance (L) of the magnetostrictive actuator measured by the Arduino based data acquisition system, the load *vs*. time data is obtained from the UTM and the crack length *vs*. time data from the video camera. Thus as the common reference for all of these is time, each data set is plotted against time, along with the normalised inductance and the rate of change of inductance (dL/dt). The required data from the datasets were interpolated to enable the correlation of each dataset to discrete time steps, through a general function $f(t)$ where t is time. Using this way of analysis, the crack position and the applied load at a particular time can be determined.

5.1. Mode 1 - interlaminar fracture due to matrix failure under tensile loading

Fig. 3a shows the graphical representation of the data for Mode 1 sample with the ribbon attached on top and Fig. 3b for the Mode 1 data for the ribbon embedded within the CFRP coupon. Fig. 3a(I) shows the data load *vs* time data obtained from the UTM. Fig. 3a(II) exhibits the raw inductance data obtained from the Arduino based data acquisition system, which is then normalised to the value at $t = 0$ for the data shown in Fig. 3a(III). To help with analysis, the rate of change of inductance (dL/dt) is plotted in Fig. 3a(IV). Fig. 3a(V) shows the crack length *vs* time data obtained from the video camera. Three vertical lines are also be observed in Fig. 3a, to divide the data into four sectors, which correspond to the sensor positions such as sensor 2, sensor 3 and sensor 4 and have been extrapolated from the crack length data, which can be seen in Fig. 3a(V).

During the initial phase of the test, a drop in the normalised inductance (*cf.* Fig. 3a(III)) can be observed. The normalised inductance value drops from 1 to 0.2 at ~250 s. This occurs because of shape deformation of the laminate during the initial loading. This can also be confirmed with the load *vs* time data (*cf.* Fig. 3a(I)). In the first sector of the load *vs* time plot, the applied load increases and reaches the maximum value before delamination. This load creates a deformation in the sample prior to delamination. This can also be reconfirmed with the crack length *vs* time plot (*cf.* Fig. 3a(V)), where no crack propagation is observed. When the sample reaches the maximum load bearing limit a drop in load is observed due to energy release, which results in delamination and crack growth. This is a common trend observed in Mode 1 fracture testing of CFRP materials.

When the crack approaches sensor 2, which is placed at 60 mm, the normalised inductance value starts decreasing from 1 to 0.2 over the time span of 300–690 s. While the normalised inductance values of sensor 3 and sensor 4 remain unchanged until the crack crosses sensor 2. When the crack propagates past sensor 2, the normalised inductance starts to decrease in sensor 3 indicating damage occurrence over that particular area. When the crack propagates furthermore towards sensor 4, the normalised inductance value gradually starts decreasing. After the crack coincides with the sensor position the normalised inductance drops to its minimal value after which it remains constant.

The rate of inductance change (dL/dt) can also be used as an aid to analyse crack propagation behaviour and is shown in Fig. 3a(IV). The minima of the (dL/dt) plots are representative of where the normalised inductance in Fig. 3a(III) drops to zero and hence where the crack has propagated past that particular sensor. The sensor positions are indicated in Fig. 3a as a function of the crack length obtained from the recorded video; these lines are in good agreement with the minimum values of the normalised inductance shown in Fig. 3a(III), validating our analysis. Additionally, the minima positions in Fig. 3a(IV) are also in agreement with the sensor positions. This is also confirmed from the recorded crack propagation footage.

Similarly, Fig. 3b represents the data of Mode 1 failure with the magnetostrictive actuator located between 8th and 9th ply of the CFRP coupon (*i.e.* in its centre), with the same data represented within the 5 graphs. On visual comparison of Fig. 3b with Fig. 3a, it can be observed that the data follows the same trend as expected. But on comparing the inductance data (*cf.* Fig. 3b(II)) and the normalised inductance (*cf.* Fig. 3b(III)) of the CFRP coupon with actuator in the middle with inductance (*cf.* Fig. 3b(II)) and the normalised inductance for the actuator on top (*cf.* Fig. 3a(III)), it can be observed that, for the CFRP coupon with actuator in the middle (*cf.* Fig. 3b) the data has a smaller SNR compared to the data for the actuator on top. In the case of the CFRP coupon with the actuator embedded on top, the sensors are directly in contact with the actuator, which results in a stronger magnetic

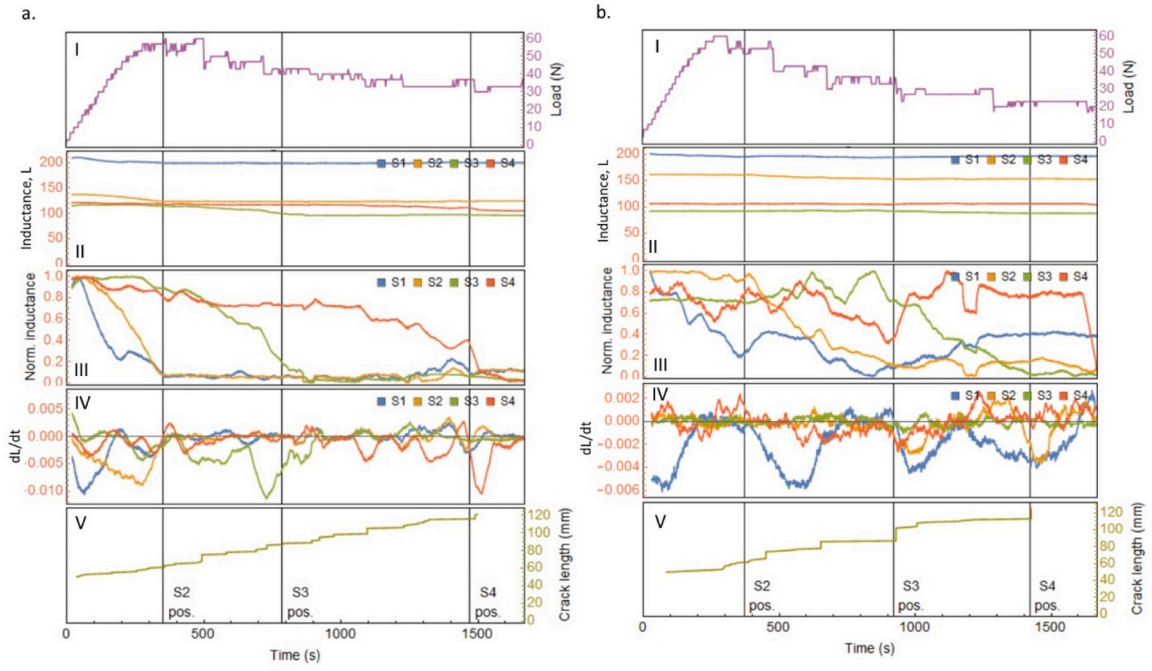

Fig. 3. a) Data for a composite coupon in Mode 1 failure setup (Ribbon on top layer); **b)** Data for a composite coupon in Mode 1 failure setup (Ribbon in middle).

interaction between the sensor and actuator and therefore a large signal compared to the noise. In the case of CFRP coupon where the actuator is sandwiched between 8th and 9th ply of the CFRP coupon, the magnetic interaction between the actuator and sensors are weaker due to the 2.24 mm thick CFRP composite between them, thus the signal measured is smaller, and hence the noise on the data noticeably larger.

Due to this weaker magnetic interaction between the sensor and the actuator the degree of change in inductance observed is smaller when compared to the data with actuator on top configuration, leading to the smaller SNR. It is suspected that the metallic parts of the UTM tensile testing fixture could contribute to the noise in the sensor data to some extent. Although there is a smaller change in inductance and a significant amount of noise in the inductance data (*cf.* Fig. 3b(II)) and normalised inductance data (*cf.* Fig. 3b(III)), the change in inductance trend can still be observed to be similar to that of the results observed with actuator on top configuration. In the normalised inductance plot (*cf.* Fig. 3b(III)) a large drop in normalised inductance value for sensor 1 can be observed when compared to sensor 2,3,4 in the first sector. This drop in normalised inductance is as result of initial loading and shape deformation occurring in the sample, which can also be correlated to the increase in load which can be observed at the first sector of load *vs* time plot (*cf.* Fig. 3b(I)). In the second sector of the normalised inductance plot a drop in inductance can be observed in the sensor 2 from 0.9 to 0.1. Similar behaviour for sensor 3 is observed in the third sector. Although sensor 4 does not have the large drop in normalised inductance as would be expected, there is a sudden drop in normalised inductance after 1600 s representing complete fracture. By comparing the change in normalised inductance data from the Mode 1 fracture tests, with the actuator configurations embedding on top of the coupon *vs.* the actuator sandwiched between the plies it can be inferred that actuator on top of the coupon generates clearer results due to a larger SNR. While, placing the actuator between the plies gave a smaller SNR, plus it would seem that the rate of crack propagation or delamination is increased due to the ribbon being between the layers [25].

5.2. Mode 2 fracture - (inter laminar fracture due to matrix failure under shear loading)

The data obtained from our Mode 2 tests are plotted using the same strategy as in the previous section and are shown in Fig. 4a (Actuator on top-layer) and 4b (Actuator in mid-layer). The major difference in the Mode 2 plots when compared to the Mode 1 plots is the three vertical lines dividing the plot into four quadrants. In Fig. 3, the plots were divided with respect to the sensor position. Similar method of analysis cannot be applied to Mode 2 since the coupons experienced catastrophic failure when the crack length reached 75 mm. Therefore, a different approach has been applied to divide the plot in four quadrants depending upon the damage occurring in the sample by combining the data obtained from the video camera and from the Arduino based data acquisition system. The first quadrant represents the initial loading where the coupon experiences only the bending stress, with no crack growth. In this region a large drop in inductance can be observed. In the second quadrant the crack propagation initiates, and the change in inductance remains almost constant. The third quadrant represents faster crack growth and multiple delaminations occurring in the stress concentrated region. These multiple delaminations cause a minor change in inductance when compared to the change in inductance observed in the crack growth region (quadrant 2). The fourth quadrant represents fracture, where a maximum change in inductance is observed.

From the normalised inductance plot in Fig. 4a(III), it can be observed that when the sample is subjected to stress there is a drop in inductance, which can be observed across all four sensors. From the normalised inductance plot in Fig. 4a(III), when stress is applied to the sample a gradual drop in inductance is observed due to the initial bending of the sample. As the crack propagates the inductance remains constant. When fracture occurs a sudden increase in inductance is observed and the inductance value is restored to the initial value. As in the previous section, the derivative of Fig. 4a(III) is used to analyse the change in inductance and how it correlates to crack growth and failure in Mode 2 failure in end-notch failure tests and by extension, samples experiencing a similar class of failure.

From Fig. 4a(IV), the (dL/dt) values increases from –0.02–0, which tracks the decrease in normalised inductance in Fig. 4a(III) well. In contrast to the fluctuations in the normalised inductance in Quadrant 2, the derivative function shows low levels of fluctuations (*cf.* Fig. 4a(IV); from this data we hypothesise the fluctuations are attributed to variations in the distance of the sensor from nearby ferrous materials (*i.e.* Due

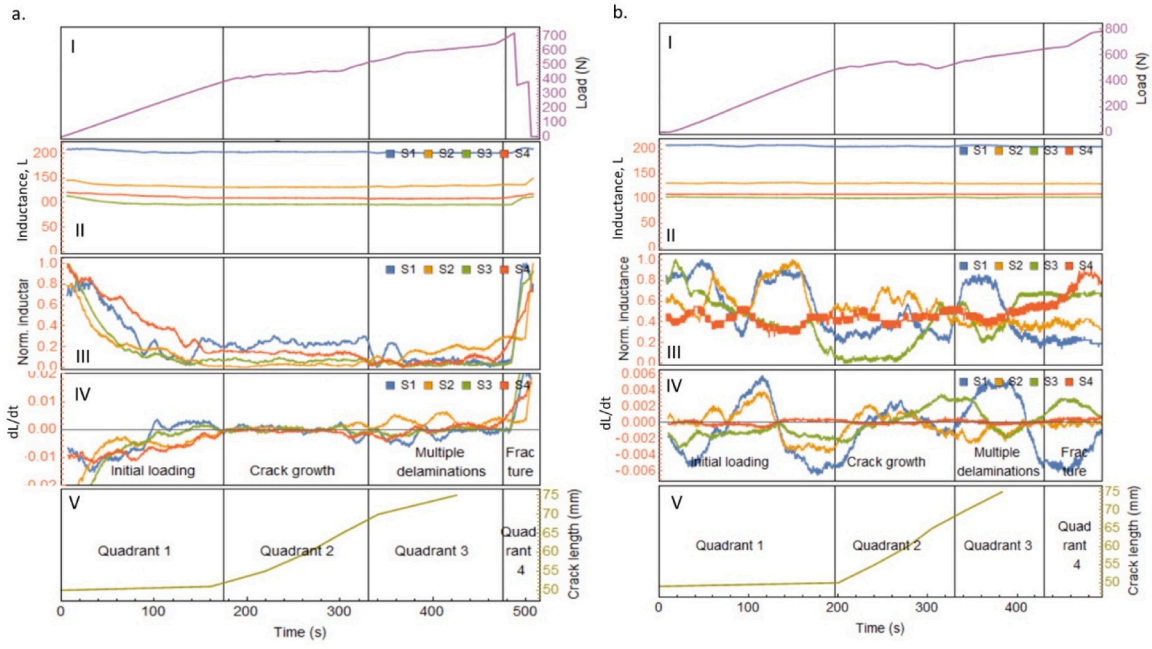

Fig. 4. a) Data for a composite coupon in Mode 2 failure setup (Ribbon on top), **b)** Data for a composite coupon in Mode 2 failure setup (Ribbon in middle).

to sample slip and/or nearby crosshead or other equipment movement). The complex behaviour happening is in contrast to the more simplistic normalised inductance behaviour in the Mode 1 tests (*cf.* Fig. 3a(III)) – this is attributed to the influence of shear on the energy stored in the sample and is discussed further in a later section.

In Quadrant 3, the sample undergoes debonding and multiple delamination before failure. The derivative curve in Fig. 4a(IV) fluctuates between –0.01 and 0.01 in contrast to the near-linear behaviour exhibited in Quadrant 2. These spikes are attributed to localised regions of stress (possibly due to inhomogeneous curing or some activation energy threshold being overcome) that build up to minor slip and delamination events that occur repeatedly before sample failure. A rapid irreversible spike in inductance is observed in Quadrant 4, which we correlated with sample failure and can be used to conclude that permanent damage has occurred within the sample.

Unlike the Mode 1 tests (*cf.* Fig. 3a(III)), it is impossible to determine the crack location with respect to each sensor position (*cf.* Fig. 4a(III)). From the video recordings, the crack length only passes by sensor 1, however all four sensors show very similar behaviour to each other that is almost indistinguishable. Analysis of the normalised inductance's derivative also shows no clear distinguishing features from each sensor readout. From this, we infer that it is likely that Mode 2 failure imposes strain across the entire coupon cross-section, in comparison to Mode 1 deformation, which has more localised stress regions. This agrees with [38].

From the observed data it can be concluded that the actuator in the middle setup does not work as well when compared to the actuator on top setup. Similar to the results observed in Mode 1, the actuator on top configuration gave the larger change in inductance with a larger SNR. Unlike Mode 1, the crack propagation could not be easily tracked in Mode 2 fracture mechanics. But the change in inductance can be used to interpret the delamination, debonding, and fracture events occurring in the coupon. This is further analysed in the section below.

6. Discussion - mechanics of failure

The results of both Mode 1 and Mode 2 failure tests are presented in Sections 4.1 and 4.2, which clearly show the differences in the measured inductance behaviour for each failure type. The challenge of SHM is not only in the determination of failure position (which can be demonstrated for Mode 1 samples from the normalised inductance derivative), but also in determining the type of failure experienced. Increased understanding of the failure mechanism is essential as this will aid in the construction of detection strategies that can be used to parse inductance results on-the-fly during essential operations that will enable SHM. In order to look into this, in the next section we present a mathematical model of the energy stored within the sample and compare it to our experimental inductance values.

6.1. Mode 1 failure

The strains in a beam in pure bending vary linearly from the neutral surface regardless of the shape of the stress strain curve of the material. The longitudinal strains in a beam are accompanied by transverse strains (normal in the y and z directions) due to the effects of the Poisson's ratio. There are accompanying transverse stresses because the beams are free to deform laterally. The longitudinal elements in a beam in pure bending are in a state of uniaxial stress. The strain-curvature relationship for such an ideal beam is $\epsilon_x = -k\,y$ where y is the distance from the central point and k is the curvature. However, the CFRP coupon in the Mode 1 setup can be thought of as two attached beams that are being pulled apart, where the CFRP coupon is only strained once the bond has failed. In Mode 1 fracture, when a tensile load is applied at the pre-cracked end of the laminate, delamination occurs as a result of matrix failure and the crack grows perpendicular to the direction of the applied load. In Mode 2 fracture when a bending load is applied to the laminate, the surface on which the load is applied experiences a compressive loading and the lower part of the laminate experiences a tensile loading. To better understand the data taken in our experiments, we calculate the strain energy release rate of the system for both Mode 1 and Mode 2 fractures.

The FeSiB actuators used here are amorphous and possess no grains for magnetic domain wall pinning, which leads to soft magnetic behaviour. As such, to simplify matters, we assume that the actuators experience reversible magnetisation. The isotropic form of the relationship between the magnetostriction ($\lambda(t, x)$) and magnetisation ($M(t, x)$) can be written as [39]:

$$\lambda(t,x) = \frac{3}{2}\quad\frac{\lambda_s}{M_s^2}M^2(t,x) \tag{2}$$

Where λ_s is the saturation magnetostriction and M_s is the saturation magnetisation. The change in inductance, ΔL for the sensor coil is proportional to:

1) The internal magnetic field strength, H,
2) The number of coil turns, N.

As no current is passed through the coils, $H = 0$ and the number of turns are kept constant for all sensors, we therefore expect $\Delta L \approx \Delta M$. Thus normalising ΔL as $\left(\frac{\Delta L - L_{Min}}{L_{Max} - L_{Min}}\right)$ provides a reasonable estimate of $\Delta M/M_s$ in the form of $\Delta L_{Norm} = \frac{\Delta M}{M_s} + C_{offset}$ where C_{offset} is an offset constant dependent on the remanent magnetisation.

Rearranging Eq. 2, we find that the magnetostriction can be written as:

$$\left[\left(\frac{2}{3}\right)\left(\frac{\lambda(t,x)}{\lambda_s}\right)\right]^{\frac{1}{2}} = \frac{M(t,x)}{M_s} \tag{3}$$

showing the quadratic relationship between the normalised magnetostriction and the normalised magnetisation.

Next, the strain release rate in an end-notched flexure for both modes can be evaluated. The Mode 1 testing is written as [40]:

$$K = \frac{\sqrt{3}}{2}\frac{Eh^{\frac{3}{2}}\delta}{a^2}\quad\left[\frac{1 + 0.64\left(\frac{h}{a}\right)}{1 + 1.92\left(\frac{h}{a}\right) + 1.22\left(\frac{h}{a}\right)^2 + 0.39\left(\frac{h}{a}\right)^3}\right] \tag{4}$$

Similar, the strain energy release rate for Mode II testing can be written as [41]:

$$G_{II}^{SH} = \frac{9a^2P^2}{16E_1w^2h^3}\left[1 + 0.2\left(\frac{E_1}{G_{13}}\right)\left(\frac{h}{a}\right)^2\right] \tag{5}$$

where P is the applied load, δ is displacement, $2h$ is height, G is interlaminar shear toughness, E is elastic modulus, a is crack length and w is the width of the sample.

The material properties required for the calculation input are obtained from the material datasheet and are tabulated in Table 2. The

Table 2
VTC401® datasheet values [33]. *The shear modulus was not given in the datasheet and was approximated from knowledge of Poisson's ratio and the elastic modulus.

Measurement	Value	Units
Compressive strength	631	MPa
Tensile strength	573	MPa
Tensile modulus	52.7	Gpa
Poisson ratio	0.053	–
DMA Tg	150	C
Flexural strength	863	MPa
Flexural modulus	51.7	GPa
Inter shear strength	74	MPa
Shear strength	74.6	MPa
Shear modulus*	25.23	GPa

shear modulus was not given and was approximated from knowledge of Poisson's ratio and the elastic modulus, assuming that the twill-weave CFRP coupons behave isotopically. Utilising Mathematica 11.0 [42], we interpolated the experimental data to determine the strain release rate, $G(II)$. These results are shown in Fig. 5a alongside the experimental crack length data determined from the video recording. The work done to deform the CFRP coupons is evaluated from the datafile as $W = F \times X$ where F is the force in Newtons and X is the height traversed. The total energy released over a given time interval may be obtained by taking the integration of the interpolated function of Eq. 4: $E_{Strain} = \int_0^n f \times A_{Crack} dt$ at each time interval, n, where A is the crack area. The time-resolution of the camera used in this work was not suitable to evaluate crack propagation mechanics before failure. As a result, the crack area is obtained by the function $A_{crack} = a \times a_{fit}$ where a_{fit} is a fitting parameter obtained by evaluating $\int_0^n f \times A_{Crack} dt = W(n)$ where n is the time just before failure at which the force is maximum. For the Mode 1 test sample, $n = 1472$and $a_{fit} = 0.0072m$, which corresponds well to the crack tip width. For the Mode 2 test sample, $n = 479$ and $a_{fit} = 0.066m$, which corresponds well to the measured crack width of 0.05 m. A visual comparison of the samples just after failure confirms that the crack tip width is much larger in Mode 2 failure. The energy stored within the sample during the evaluation process is evaluated as:

$$\Delta E = W - E_{Strain} \tag{6}$$

For our installed magnetostrictive actuator/sensor setup to accurately pick up changes in strain, we would therefore expect $\sqrt{\Delta E} \approx \Delta L$.

From the calculated strain energy release rate data and crack propagation data, the strain energy increases due to the bending stress in the initial phase. As the crack propagates and the CFRP coupon loses its strength, the strain energy starts decreasing, which reflects the failure of the CFRP coupon. When the coupon approaches failure, the energy required for crack propagation decreases, and the total energy in the sample exceeds representing failure. Fig. 5a and b shows the energy change *vs* time data for both Mode 1 and 2. It can be observed that the energy change *vs.* time data can be compared with the normalized inductance data in Fig. 3a(III). From the graph, it can be observed that the normalized inductance values almost drop to 0 at around 200 s, when compared with the calculated magnetostrictive data, where the magnetostriction values dropped and reached a minimum level in a similar time. From this it can be concluded that the calculated values are in accordance with the experimental values.

Shear stress also plays an important role in Mode 2 fracture test. When the laminate is strained, due to the shear force acting along the pre crack the laminate starts to delaminate. The crack propagates much faster when compared to Mode 1. When the crack reaches the point where the load is applied due to high stress concentration over that area due to the bending stress and the shear force, multiple debonding and delamination occur. The laminate experiences a catastrophic failure. These correspond to the regions 1, 2, and 3 shown in Fig. 4 and are in

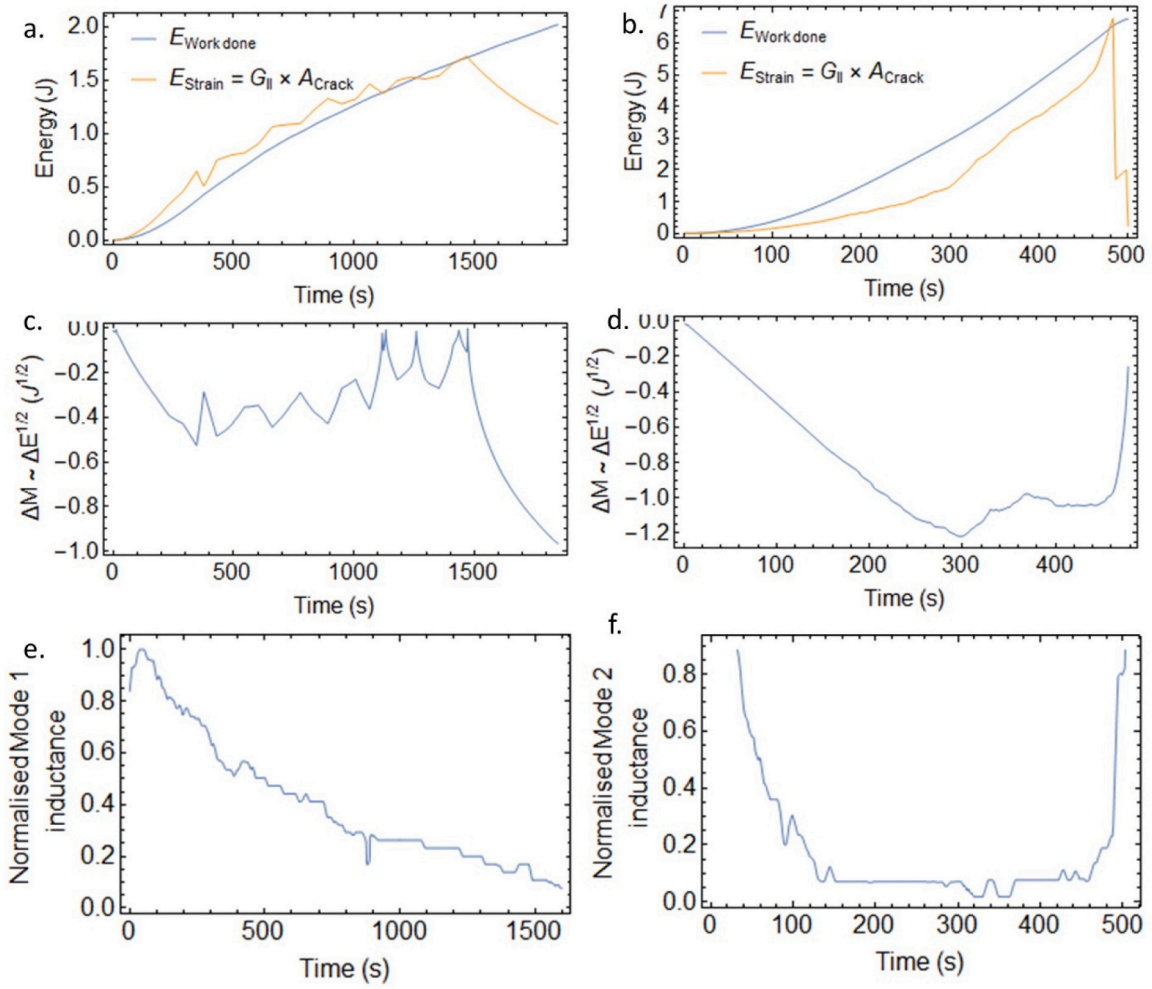

Fig. 5. **a)** Strain energy release rate *vs.* time for Mode 1, **b)** Strain energy release rate *vs.* time for Mode 2, **c)** Energy change *vs.* time for Mode 1, **d)** Energy change *vs.* Time for Mode 2, **e)** Inductance response normalised across all four sensors for Mode 1, **f)** Inductance response normalised across all four sensors for Mode 2.

agreement with our energy analysis. For comparison, we show the inductance response normalised across all four sensors for Mode 1 and Mode 2 in Fig. 5e and f. The results are thus in good agreement with the data.

The mathematical models of the strain evolution in the CFRP coupons can thus be built into smart magnetostrictive detection schemes (using signal processing strategies) to characterise and differentiate between the types of failure that is occurring in CFRP coupons.

7. Conclusions

The main goal of the study was to investigate the effectiveness of the magnetostrictive based structural health monitoring system [9] in detecting Mode 1 and Mode 2 delamination in CFRP coupons. The research also investigated the efficacy of actuator placement between plies and its implications on the data obtained from the sensor and data acquisition system. From this research, the results have indicated that crack propagation can be easily monitored with the change in inductance in the case of Mode 1 fracture. Once the coupon is strained a drop in inductance is observed in the sensors. This drop in inductance can be correlated to the crack position. A drop in inductance from a specific sensor represents the crack propagation in the vicinity of the sensor. The findings also suggest in general that the actuator placement between the plies is not the best option since it had a lower SNR compared to the actuator on top configuration. In case of Mode 2 fracture, using the change in inductance along with data analysis, the type of damage occurring to the CFRP coupon has been established. Similar to the Mode 1, embedding the actuator on top of the coupon provides a larger SNR compared to placing the actuator between the plies. The major limitation in case of Mode 2 fracture is that the crack propagation cannot be easily interpreted with the change in inductance data due to its complex bending and shear component involvement. In spite of this limitation the normalised inductance data and dL/dt data have shown the events that happen in the coupon such as loading, crack growth, multiple delamination, and fracture. The other significant finding in this study is that the strain energy release can be correlated to the change in inductance occurring in the sensor. This will lead to the development of magnetostrictive SHM systems along with signal processing strategies which aid to understand the damage occurring in composite structures.

CRediT authorship contribution statement

JDS Vincent: Software, Analysis, Investigation, Data Curation, Writing – Original Draft, Visualization; **Z Leong:** Conceptualisation, Methodology, Software, Validation, Formal Analysis, Writing – Original Draft, Writing – Review & Editing, Visualization, Supervision; **N Morley:** Resources, Writing – Review & Editing, Supervision, Project administration, Funding acquisition.

Declaration of Competing Interest

The authors declare that they have no known competing financial interests or personal relationships that could have appeared to influence the work reported in this paper.

Data Availability

Data will be made available on request.

Acknowledgements

ZYL would like to acknowledge Dr. Pratik Desai for his invaluable discussions, Mr. Mark McIntosh for his contribution in designing and fabricating the data acquisition system, and Mr. Jack Leach for his help in composite fabrication. This work was funded under the Cleansky2 scheme, for the project SHERLOC JTI-CS-2009-01-GRA-01-005.

Appendix A. Supporting information

Supplementary data associated with this article can be found in the online version at doi:10.1016/j.sna.2023.114888.

References

[1] S. Sgouridis, P.A. Bonnefoy, R.J. Hansman, Air transportation in a carbon constrained world: long-term dynamics of policies and strategies for mitigating the carbon footprint of commercial aviation, Transp. Res. Part A Policy Pract. 45 (10) (2011) 1077–1091, https://doi.org/10.1016/j.tra.2010.03.019.
[2] Introduction to aerospace materials, Introduction to Aerospace Materials, Elsevier,, 2012, pp. 1–14.
[3] A.C. Garg, Delamination-a damage mode in composite structures, Eng. Fract. Mech. 29 (5) (1988) 557–584, https://doi.org/10.1016/0013-7944(88)90181-6.
[4] X. Chen, H. Ren, C. Bil, Inspection intervals optimization for aircraft composite structures considering dent damage, J. Aircr. 51 (1) (2014) 303–309, https://doi.org/10.2514/1.C032377.
[5] "AC 20–107B - Composite Aircraft Structure," *Fed. Aviat. Adm.*, [Online]. Available: ⟨https://www.faa.gov/regulations_policies/advisory_circulars/index.cfm/go/document.information/documentID/99693⟩.
[6] N. Yue, Z.S. Khodaei, M.H. Aliabadi, Damage detection in large composite stiffened panels based on a novel SHM building block philosophy, Feb 2021, Smart Mater. Struct. 30 (4) (2021), 045004, https://doi.org/10.1088/1361-665X/abe4b4.
[7] F. Lambinet, Z.S. Khodaei, Measurement platform for structural health monitoring application of large scale structures, Measurement 190 (2022), 110675, https://doi.org/10.1016/j.measurement.2021.110675.
[8] Z.S. Khodaei, F.M.H. Aliabadi, Structural health monitoring of aerospace composites. Comprehensive Structural Integrity (Second Edition), Elsevier,, 2023, pp. 24–52, https://doi.org/10.1016/B978-0-12-822944-6.00046-3.
[9] J.D.S. Vincent, M. Rodrigues, Z. Leong, N.A. Morley, Design and development of magnetostrictive actuators and sensors for structural health monitoring, Sensors 20 (3) (2020) 711, https://doi.org/10.3390/s20030711.
[10] Z. Leong, W. Holmes, J. Clarke, A. Padki, S. Hayes, N.A. Morley, Magnetostrictive sensors for composite damage detection and wireless structural health monitoring, IEEE Trans. Magn. 55 (7) (2019) 1–6, https://doi.org/10.1109/TMAG.2019.2899537.
[11] Z. Leung *et al.*, "Structural Health Monitoring using magnetostrictive sensors," in *2017* IEEE International Magnetics Conference (INTERMAG), Apr. 2017, pp. 1–1, doi: 10.1109/INTMAG.2017.8007893.
[12] I. Murgulescu, et al., Magnetostrictive materials for aerospace applications, J. Phys. Conf. Ser. 903 (2017), 012010, https://doi.org/10.1088/1742-6596/903/1/012010.
[13] J. Surakarnkha, L. Zhaoyuan, P. Gong, W. Holmes, P. Desai, J. Foreman, N. Morley, Designing ferrite impregnated epoxy actuators for impact damage detection in carbon fibre reinforced composites, Compos. Sci. Technol. 216 (2021), 109085, https://doi.org/10.1016/j.compscitech.2021.109085.
[14] S.G. Taylor, G. Park, K.M. Farinholt, M.D. Todd, Diagnostics for piezoelectric transducers under cyclic loads deployed for structural health monitoring applications, Smart Mater. Struct. 22 (2) (2013), 025024, https://doi.org/10.1088/0964-1726/22/2/025024.
[15] R. Di Sante, Fibre optic sensors for structural health monitoring of aircraft composite structures: recent advances and applications, Sensors 15 (8) (2015) 18666–18713, https://doi.org/10.3390/s150818666.
[16] H. Tsutsui, A. Kawamata, T. Sanda, N. Takeda, Detection of impact damage of stiffened composite panels using embedded small-diameter optical fibers, Smart Mater. Struct. 13 (6) (2004) 1284–1290, https://doi.org/10.1088/0964-1726/13/6/002.
[17] G. Sha, C.J. Lissenden, Modeling magnetostrictive transducers for structural health monitoring: ultrasonic guided wave generation and reception, Sensors 21 (2021) 7971, https://doi.org/10.3390/s21237971.
[18] C. Xie, T. Liu, C. Pei, Z. Chen, A flexible thin-film magnetostrictive patch guided-wave transducer for structural health monitoring, IEEE Sens. J. 22 (12) (2022) 12237–12244, https://doi.org/10.1109/JSEN.2022.3174353.
[19] Y.J. Yan, L.H. Yam, Online detection of crack damage in composite plates using embedded piezoelectric actuators/sensors and wavelet analysis, Compos. Struct. 58 (1) (2002) 29–38, https://doi.org/10.1016/S0263-8223(02)00043-0.
[20] Z. Su, X. Wang, Z. Chen, L. Ye, D. Wang, A built-in active sensor network for health monitoring of composite structures, Smart Mater. Struct. 15 (6) (2006) 1939–1949, https://doi.org/10.1088/0964-1726/15/6/050.
[21] R. Ramly, W. Kuntjoro, M.K.A. Rahman, Using embedded fiber Bragg grating (FBG) sensors in smart aircraft structure materials, Procedia Eng. 41 (2012) 600–606, https://doi.org/10.1016/j.proeng.2012.07.218.
[22] J. Kratz, P. Hubert, Vacuum-bag-only co-bonding prepreg skins to aramid honeycomb core. Part II. In-situ core pressure response using embedded sensors, Compos. Part A Appl. Sci. Manuf. 72 (2015) 219–227, https://doi.org/10.1016/j.compositesa.2014.11.030.
[23] G. Luyckx, et al., Response of FBGs in microstructured and bow tie fibers embedded in laminated composite, IEEE Photonics Technol. Lett. 21 (18) (2009) 1290–1292, https://doi.org/10.1109/LPT.2009.2025262.
[24] S. Takeda, T. Tsukada, S. Sugimoto, Y. Iwahori, Monitoring of water absorption in CFRP laminates using embedded fiber Bragg grating sensors, Compos. Part A Appl. Sci. Manuf. 61 (2014) 163–171, https://doi.org/10.1016/j.compositesa.2014.02.018.

[25] M. Torres, R.A. Tellez, H. Hernández, T. Camps, Mode I interlaminar fracture toughness of carbon-epoxy coupons with embedded ceramic sensors, Adv. Polym. Technol. 37 (6) (2018) 2294–2302, https://doi.org/10.1002/adv.21905.
[26] S. Mall, T.L. Hsu, Electromechanical fatigue behaviour of graphite/epoxy laminate embedded with piezoelectric actuator, Smart Mater. Struct. 9 (1) (2000) 78–84, https://doi.org/10.1088/0964-1726/9/1/308.
[27] S. Mall, Integrity of graphite/epoxy laminate embedded with piezoelectric sensor/actuator under monotonic and fatigue loads, Smart Mater. Struct. 11 (4) (2002) 527–533, https://doi.org/10.1088/0964-1726/11/4/307.
[28] J. Hansen, A. Vizzini, J. Hansen, and A. Vizzini, "Fatigue response of a host structure with interlaced embedded devices," Apr. 1997, doi: 10.2514/6.1997–1346.
[29] L. Yao, R.C. Alderliesten, R. Benedictus, Interpreting the stress ratio effect on delamination growth in composite laminates using the concept of fatigue fracture toughness, Compos. Part A Appl. Sci. Manuf. 78 (2015) 135–142, https://doi.org/10.1016/j.compositesa.2015.08.005.
[30] A.B. Pereira, A.B. de Morais, Mixed mode I+II interlaminar fracture of carbon/epoxy laminates, Compos. Part A Appl. Sci. Manuf. 39 (2) (2008) 322–333, https://doi.org/10.1016/j.compositesa.2007.10.013.
[31] P. Robinson, J.M. Hodgkinson, Interlaminar fracture toughness. Mechanical Testing of Advanced Fibre Composites, Elsevier,, 2000, pp. 170–210.
[32] L.A. Carlsson, D.F. Adams, R.B. Pipes, Experimental Characterization of Advanced Composite Materials, CRC Press,, 2014.
[33] SHD Composites, "VTC401 Epoxy Component Prepreg," no. February, pp. 1–3, 2018, [Online]. Available: http://shdcomposites.com/wp-content/uploads/2016/03/MTC801-TDS.pdf.
[34] ASTM, "Standard test method for mode I interlaminar fracture toughness of unidirectional fiber-reinforced polymer matrix composites 1," *Annu. B. ASTM Stand.*, vol. 01, pp. 1–12, 2001, doi: 10.1520/D5528–13.2.
[35] ASTM D7905/7905M-14, "Standard Test Method for Determination of the Mode II Interlaminar Fracture Toughness of Unidirectional Fiber-Reinforced Polymer," *Am. Soc. Test. Mater.*, pp. 1–18, 2014, doi: 10.1520/D7905.
[36] A. Gullapalli, V. Beedasy, J.D.S. Vincent, Z. Leong, P. Smith, N. Morley, Flat inkjet-printed copper induction coils for magnetostrictive structural health monitoring: a comparison with bulk air coils and an anisotropic magnetoresistive sensor (AMR) sensor (org/), " Adv. Eng. Mater. 23 (2021) 2100313, https://doi.org/10.1002/adem.202100313.
[37] N. Ahmed, R. Deffley, B. Kundys, N.A. Morley, 3D printing of magnetostrictive property in 17/4 ph stainless steel, 171115-171115, Nov 2023, doi: org/, J. Magn. Magn. Mater. 585 (2023), https://doi.org/10.1016/j.jmmm.2023.171115.
[38] M.J. Laffan, Testing the toughness of polymer matrix composites. Failure Mechanisms in Polymer Matrix Composites, Elsevier,, 2012, pp. 110–128.
[39] M.J. Dapino, R.C. Smith, A.B. Flatau, Structural magnetic strain model for magnetostrictive transducers, IEEE Trans. Magn. 36 (3) (2000) 545–556, https://doi.org/10.1109/20.846217.
[40] M.F. Kanninen, An augmented double cantilever beam model for studying crack propagation and arrest, Int. J. Fract. 9 (1) (1973) 83–92, https://doi.org/10.1007/BF00035958.
[41] L.A. Carlsson, J.W. Gillespie, R.B. Pipes, On the analysis and design of the end notched flexure (ENF) specimen for mode II testing, J. Compos. Mater. 20 (6) (1986) 594–604, https://doi.org/10.1177/002199838602000606.
[42] I.Wolfram Research, "Mathematica." Wolfram Research, Inc., Champaign, Illinois, 2020, [Online]. Available: https://www.wolfram.com/mathematica.

Prof Nicola Morley, is a professor of Materials Physics at the University of Sheffield, UK. Her research focuses on the design, fabrication and characterisation of functional magnetic materials for applications, including magnetostrictive materials for structural health monitoring of aircraft and magnetocaloric materials for refrigeration. More recently she has combined machine learning with high-throughput combinatorial experiments to explore the vast compositional phase space of high entropy alloys looking for the next new soft magnetic material. Since July 2023, she has been head of the Materials Science and Engineering department at the University of Sheffield.